Corrosion Science 174 (2020) 108850

Contents lists available at ScienceDirect

Corrosion Science

journal homepage: www.elsevier.com/locate/corsci

Formation of corrosion products on zinc in wet supercritical and subcritical CO_2: In-situ spectroscopic study

A. Kaleva[a,*], T. Tassaing[b], V. Saarimaa[c], G. Le Bourdon[b], P. Väisänen[d], A. Markkula[d], E. Levänen[a]

[a] Unit of Materials Science and Environmental Engineering, Tampere University, P.O. Box 589, FI-33101 Tampere, Finland
[b] Institut des Sciences Moléculaires, UMR 5255 CNRS-Université de Bordeaux, 351 Cours de la Libération, 33405 Talence Cedex, France
[c] Top Analytica, Ruukinkatu 4, FI-20540 Turku, Finland
[d] SSAB Europe, Harvialantie 420, FI-13300 Hämeenlinna, Finland

ARTICLE INFO

Keywords:
Zinc
Raman spectroscopy
IR spectroscopy
SEM
Oxidation
Acid corrosion

ABSTRACT

Formation of corrosion products on zinc was investigated with in-situ Raman and FTIR when exposed to wet supercritical carbon dioxide ($scCO_2$) and subsequent depressurization. Zinc oxide (ZnO) and smithsonite ($ZnCO_3$) formed on zinc in $scCO_2$. The dissolved water precipitated as liquid water in the reaction cell during depressurization. Formation of ZnO, $ZnCO_3$ and a needle-like zinc hydroxy carbonate species on zinc was observed inside a sessile water droplet during conditions simulating the depressurization phase. Addition of oxygen accelerated the formation of the carbonate species due to higher cathodic activity that increased zinc dissolution.

1. Introduction

Zinc is widely used for corrosion protection in galvanized steels by providing sacrificial protection. The surface of galvanized steel typically has poor adhesion to organic coatings and requires an adhesion layer that is currently obtained by chemical surface treatments of zinc within the industry [1,2]. However, the chemicals used in the treatments are harmful for the environment, which has led to the search of alternative methods [3,4]. Carbonates formed on zinc surfaces due to atmospheric corrosion have shown exceptional improvement in corrosion resistance of zinc, as well as better adhesion for organic coatings that are later applied [5–9]. Therefore, artificially grown carbonate layer produced with a $scCO_2$-treatment method would provide advantageous surface properties as shown in our previous studies [10,11]. The present study aims to investigate in detail the interactions of zinc, CO_2 and water that occur in the wet supercritical and subcritical CO_2 conditions during the treatment.

Zinc carbonates are insoluble corrosion products that form when metallic zinc is exposed to atmospheric CO_2 and humidity. Examples of these carbonates are, e.g. hydrozincite ($Zn_5(CO_3)_2(OH)_6$), other zinc hydroxy carbonates and smithsonite ($ZnCO_3$) [12,13]. The formation of the naturally grown carbonates starts by reactions between zinc, oxygen and water that form initial corrosion products such as zinc oxide (ZnO) and zinc hydroxide ($Zn(OH)_2$) [14]. As atmospheric CO_2 dissolves into rainwater and air humidity, it reacts with water to form carbonic acid (H_2CO_3). Carbonic acid further dissociates into bicarbonate (HCO_3^-) and carbonate (CO_3^{2-}) ions that react with the initial corrosion products to form zinc carbonates when the water is in contact with the zinc surface [7,14]. The water layer will then dry in air and subsequently wet again in a repeating cyclical process and results in better coverage of the carbonate layer on zinc [7,15]. However, this process could take up to two years for a fully-developed carbonate layer to form before the application of organic coatings is viable [5]. Consequently, an accelerated carbonate formation process would be effective.

The concentration of CO_2 is one of the limiting factors in zinc carbonate formation [16]. When CO_2 is heated and pressurized, it becomes supercritical with a vastly higher concentration of CO_2 compared to the atmosphere [17]. Supercritical CO_2 ($scCO_2$) is also capable of dissolving water which allows water to react with substances in the entire volume of the reaction cell. Furthermore, carbonates are shown to form on mineral surfaces, i.e. magnesium silicates, as well as steel surfaces when exposed to $scCO_2$ saturated with water [18–20].

We previously observed the formation of carbonate structures on galvanized steel in a wet $scCO_2$ treatment and showed its viability as a pretreatment method before organic coating application [10,11]. While the applicability of this treatment has already been demonstrated, more information on the formation process needs to be obtained for a fundamental understanding of the treatment process. This study investigated the interactions between zinc, water and pressurized CO_2 in

* Corresponding author.
E-mail address: aaretti.kaleva@tuni.fi (A. Kaleva).

https://doi.org/10.1016/j.corsci.2020.108850
Received 14 April 2020; Received in revised form 9 June 2020; Accepted 30 June 2020
Available online 04 July 2020

the wet $scCO_2$ phase as well as in the presence of a liquid water layer under subcritical CO_2 conditions. The formation of zinc carbonates on the zinc surface was measured during the wet $scCO_2$ treatment by in-situ Raman and FTIR methods. The interactions of a liquid water layer on zinc was studied with sessile droplet tests with in-situ Raman. Furthermore, the effect of oxygen on corrosion product formation was investigated.

2. Materials and methods

The substrate material used was zinc sheet (99,9 m-%. Alfa Aesar) that was cut into circular specimens (d = 12 mm). Two holes (d = 1 mm) were drilled into the specimens to allow CO_2 to enter between the sample and window in the cell setup. The specimen surfaces were ground and polished with silicon carbide paper to a mirror finish and ultrasonically cleaned in ethanol to prevent oxidation. CO_2 (99.95 %) and O_2 (99.99 %) were obtained from Air Liquide. All experiments were conducted in a stainless-steel cell with a volume of 5.4 mL [21].

2.1. Wet $scCO_2$ tests (in-situ Raman and FTIR)

Raman and FTIR are distinguished methods for in-situ investigation of carbonate formation [22,23]. The schematic of the sample setup of the $scCO_2$ experiments can be seen from Fig. 1. The samples were fixed into the cell parallel to the measurement window. In-situ Raman and FTIR measurements were done for the $scCO_2$ experiments. Signals were recorded through the window, as presented in Fig. 1. Water and a magnetic stirrer were placed in a container at the bottom of the cell. The amount of water (0.2 mL) used in the experiments was in excess of what $scCO_2$ can dissolve at the chosen treatment conditions [24]. The water in the $scCO_2$ tests was placed in a distant container inside the cell to ensure no liquid water emulsion droplets could contact the sample surface. The setup of the cell was the same for measurements in both Raman and FTIR except for different window material. Sapphire was used for the Raman experiments and Calcium fluoride (CaF_2) for the FTIR measurements because of sapphire's high absorption of infrared radiation in the measurement range.

The treatments were conducted under a CO_2 pressure of 100 bar with two different sample temperatures of 40 °C and 60 °C. Specimens were kept in static conditions for 120 min after which the reaction cell was slowly depressurized for 15 min. Separate samples were exposed for in-situ Raman and in-situ FTIR measurements. The total amount of samples was four, as seen in Table 1.

The in-situ spectra for the FTIR measurements in Fig. 8 were processed due to multiple overlapping peaks between reaction species. Consequently, the influence of CO_2 and dissolved water was mitigated by subtracting the 10-minute spectrum from the subsequent measurement spectra. The subtraction helps to detect the time-dependent structural changes on the zinc surface without the influence of the surrounding $scCO_2$ phase.

Table 1
Sample conditions for the $scCO_2$ tests.

	100 bar CO_2	
40 °C	Raman	FTIR
60 °C	Raman	FTIR

2.2. Sessile droplet tests (in-situ Raman)

The sample schematic for the sessile droplet experiments can be seen in Fig. 2. In-situ Raman measurements and optical imaging were conducted for the droplet experiments. The sample was fixed to the cell similarly to $scCO_2$ experiments except for a longer distance between the sample and window to eliminate contact between droplet and window. The experiments were conducted by placing the droplet on the sample surface before transferring it to the cell setup. The sample with the droplet was quickly moved to the experimental setup to start the experiment to prevent oxidation before introducing the gases. The surface of the zinc under the droplet was measured with Raman prior to the experiment to ensure no oxidation had occurred. The droplet size used in all experiments was 3 µL (D = 2.19 ± 0.06 mm). The optical images were taken from the middle of the droplet for each test. Sapphire window was used for the experiments.

The experiment conditions of the droplet tests was temperature of 22 °C (room temperature) in 5 bar CO_2 pressure. The tests were performed without extra oxygen (Sample A) and with additional 2 bar of O_2 (Sample B) as shown in Table 2.

2.3. Characterization

Scanning electron microscopy (SEM) characterization was performed with JEOL JSM-IT500 together with integrated EDS detector (JEOL, silicon drift detector). The samples were also characterized with XRD (Panalytical Empyrean, monochromatized CuKα radiation, $5 < 2\theta < 80$) by using grazing incidence measurement (GIXRD) to focus the analysis on the topmost layer of the samples.

The Raman experiments were done using Jobin-Yvon Horiba XploRA confocal Raman microscope equipped with a 50X objective and a laser diode with a maximum power of 45 mW [21]. The spectral range of 200 – 1900 cm^{-1} was recorded with a grating of 1800 l/mm and resolution of 4 cm^{-1}. The measurements used λ = 532 nm wavelength

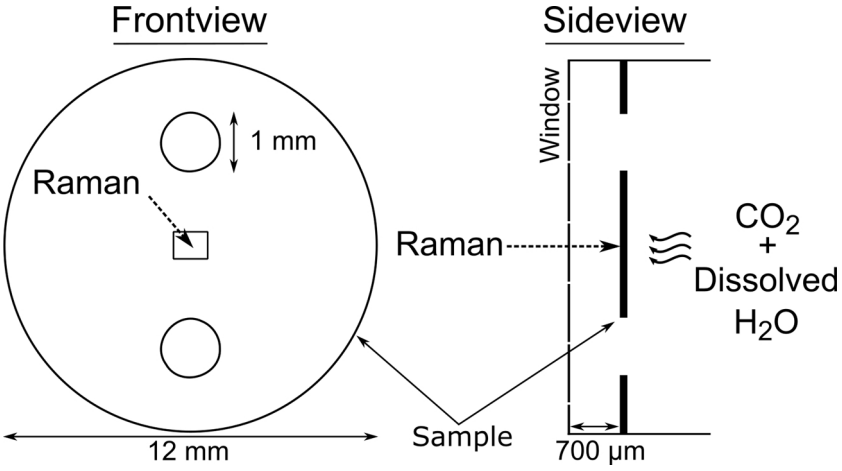

Fig. 1. Schematic of the sample setup in the wet $scCO_2$ tests.

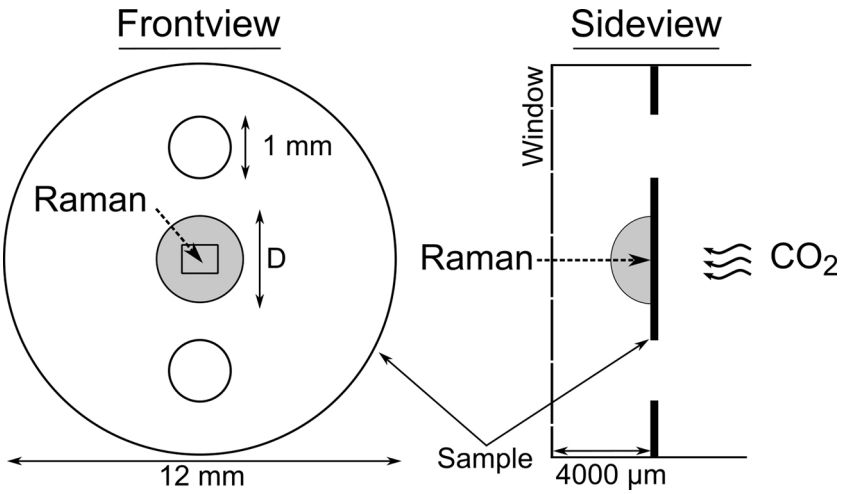

Fig. 2. Schematic of the sample setup in the droplet tests.

Table 2
Sample conditions for the sessile droplet tests.

	5 bar CO_2	5 bar CO_2 2 bar O_2
22 °C	Sample A	Sample B

and 100 % laser power. Two 60 s spectra acquisitions were taken for each measurement to improve the signal-to-noise ratio.

The infrared experiments were performed using an FTIR microscope working in transflection mode coupled with a high-pressure cell [25]. The FTIR microscope consists in a ThermoOptek interferometer (type 6700) with a globar source and KBr/Ge beamsplitters coupled to an infrared microscope (NicPlan, Nicolet) equipped with a 15X cassegrain objective and an MCT (Mercury Cadmium Telluride) detector to investigate the spectral range from 400 to 7500 cm^{-1}. Single beam spectra recorded with a 2 cm^{-1} resolution were obtained after the Fourier transformation of 32 accumulated interferograms.

3. Results and discussion

3.1. In-situ wet $scCO_2$ tests (Raman and FTIR)

The optical images that were taken during the in-situ Raman tests in wet $scCO_2$ (Fig. 3) show the appearance of dark spatters on the Zn-surface due to the wet $scCO_2$ treatment at both treatments performed in 40 °C and 60 °C. The zinc surface is rapidly covered with the spatters at 40 °C in the first 30 min, and continue to significantly increase in quantity by the end of the treatment. The 60 °C sample showed a similar behaviour as the 40 °C sample but with considerably less change on the surface. The dark spatters indicate the early stages of corrosion on the zinc surface, which is initiated by the dissolved water in the $scCO_2$ phase as no free water is present.

The Raman spectra taken from designated spots shown in the optical images (white circles) can be seen in Fig. 4. The weak peaks observed between 400 – 500 cm^{-1} and at 730 cm^{-1} that are present in all in-situ spectra (5–120 minutes) are due to the sapphire window used in the experiments. There is no noticeable Raman signal during the first 90 min in either sample even though there was an apparent visual change on the surfaces as seen from Fig. 3. At 120 min, the Raman spectrum of the 40 °C sample indicates the presence of $ZnCO_3$ due to ν_1 symmetric stretching mode at 1093 cm^{-1} and lattice mode at 300 cm^{-1} [26]. In the 60 °C sample, no carbonate peaks could be detected in the in-situ spectra, but a broad and small intensity peak at 570 cm^{-1} appears at 120 min. Earlier studies suggest that this peak corresponds to nanosized zinc oxide (ZnO) [14,27,28]. ZnO is generally considered to be an intermediate reaction step before the formation of carbonate species or other zinc corrosion products [7,17]. The ZnO formation in these experiments could be due to the reaction between zinc and dissolved oxygen that forms $ZnCO_3$ in subsequent reactions with CO_3^{2-} and HCO_3- ions. The oxygen could derive from the remaining dissolved oxygen in the water or the air confined inside the cell.

The ex-situ spectra were taken after the experiments from the sample surfaces without the measurement window. Both samples show peaks at 1093 cm^{-1}, 300 cm^{-1} and a new peak at 730 cm^{-1} which is the ν_4 antisymmetric bending mode of $ZnCO_3$ [26]. The samples also show a broad peak at around 570 cm^{-1} with an intensity that varied

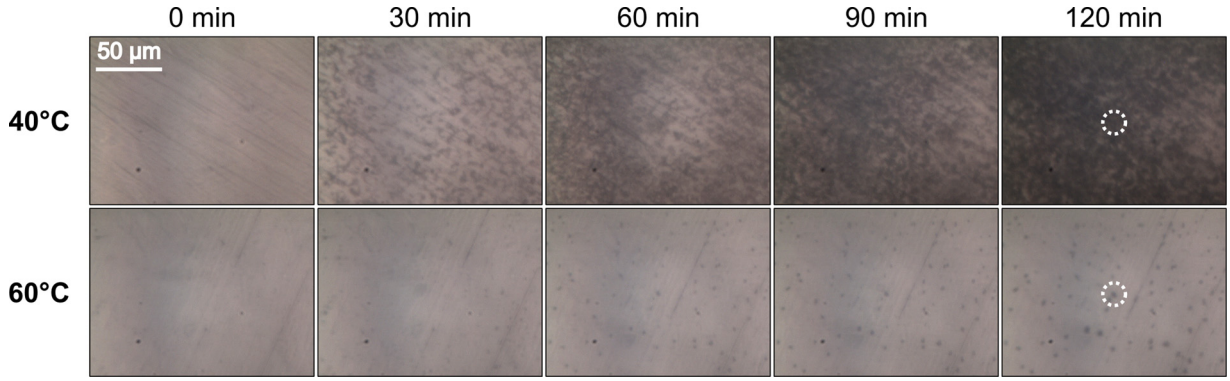

Fig. 3. In-situ optical images of Zn samples in wet $scCO_2$ at 100 bar pressure and treatment temperatures of 40 °C and 60 °C. The circles indicate the area where the Raman signal was measured (2 µm Raman spot size).

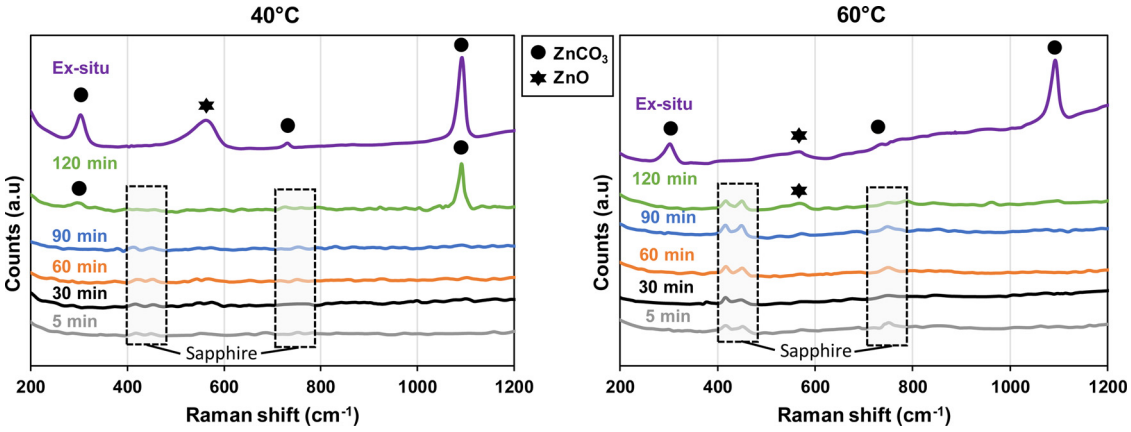

Fig. 4. In-situ and ex-situ Raman spectra of Zn samples in wet $scCO_2$ at 100 bar pressure and treatment temperatures of 40 °C and 60 °C.

independently compared to other peaks when measured from multiple places. The presence of the peak is likely due to residues of the initial corrosion product, ZnO, that did not react further to form carbonates.

The dark spatters that initially grew on the surface (Fig. 3) could be corrosion pits where initial zinc corrosion products formed. It is unambiguous from the 40 °C sample that $ZnCO_3$ does eventually form in the dark spatters either directly or through intermediate species, e.g. ZnO, as a result of corrosion in wet $scCO_2$. The growth of the carbonate is also supported by the carbonate seen in the 60 °C sample even though no signal was detected during the in-situ experiment. The amount of the reaction products could likely be negligible for Raman to detect the carbonate species until a sufficient amount formed.

The SEM images in Fig. 5 show the morphology of the carbonate structures after the treatments in 40 °C (a) and 60 °C (b). Irregularly shaped carbonate structures formed on the 40 °C sample similar to the spherical structures with fine cubic features that we reported in our earlier studies [11]. The 60 °C sample shows dark spatters on the surface, which could indicate the initial stages of corrosion product formation. Both the structures seen in 40 °C and darker areas in 60 °C were identified with ex-situ Raman measurements as $ZnCO_3$ with traces of ZnO (Fig. 4). The EDS measurements showed the presence of only zinc, carbon and oxygen in the structures in both samples (not shown).

Based on the SEM and optical images as well as the in-situ Raman data, it is evident that the amount of reaction products is higher in the 40 °C sample compared to the 60 °C sample, which could be due to the differences in the amount of dissolved water at different temperatures. The absolute amounts of dissolved water in $scCO_2$ (Fig. 6) in our treatment conditions were calculated by implementing EOS-equations derived by Spycher et al. [24].

The increased amount of dissolved water in the $scCO_2$ phase will likely enhance the formation of reaction products on zinc, which is shown to be the case for steel in wet $scCO_2$ atmosphere [29,30]. The reaction dynamics of the carbonate formation could be affected by thermodynamic considerations as well due to the temperature difference. However, corrosion studies of zinc at atmospheric conditions show more corrosion in higher rather than lower temperatures, oppositely as observed in the $scCO_2$ tests [7,31]. Therefore, the effect of dissolved water amount is likely a more significant factor for the carbonate formation, although temperature itself might still have an

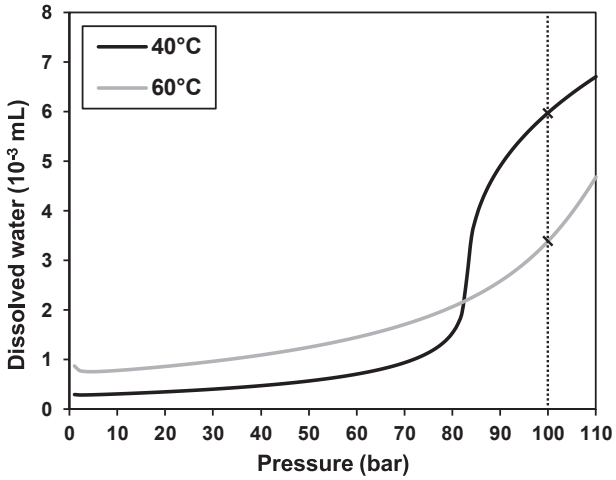

Fig. 6. The absolute amount of dissolved water in the $scCO_2$ according to the EOS-calculations using equations derived by Spycher et al. [24].

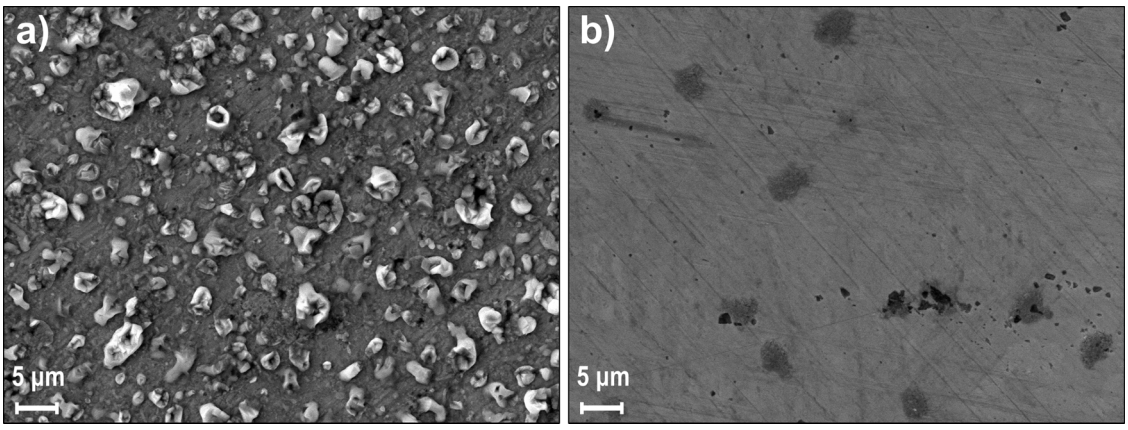

Fig. 5. SEM images of the Raman samples a) 40 °C and b) 60 °C.

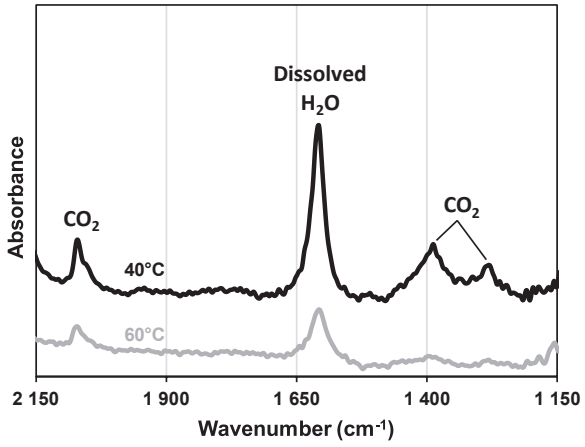

Fig. 7. In-situ FTIR spectra at 10-minute holding time of Zn samples in wet $scCO_2$ at 100 bar pressure and treatment temperatures of 40 °C and 60 °C.

impact on the reactions.

The in-situ FTIR experiments were performed with the same treatment parameters and in the same pressure cell as the in-situ Raman experiments. The goal of the FTIR measurements was to measure a larger representative area (100μm × 100μm) of the sample surfaces in contrast to the single point measurements (2μm × 2μm) done in the Raman studies. Furthermore, the presence of dissolved water and liquid water could be determined much more accurately. The FTIR spectra were recorded in the range of 1150 – 2150 cm^{-1} for the treatments in both temperatures. The measurement spectra after 10 min can be seen from Fig. 7. The peaks of CO_2 shown in the spectra at 2000 – 2150 cm^{-1} are assigned to a combination mode of the OCO bend (ν_2), and the symmetric stretch (ν_1) and the Fermi resonance peaks at 1387 cm^{-1} and mode 1281 cm^{-1} are respectively assigned to the symmetric stretching mode (ν_1) and the overtone of the OCO bending mode ($2\nu_2$). The peak at 1607 cm^{-1} is from HOH bending mode of dissolved water in the $scCO_2$ phase [32]. At 10 min treatment time, only CO_2 and dissolved water were detected in the FTIR spectra.

The intensity of the dissolved water peak correlates directly with the amount of dissolved water in CO_2 [32]. It can be seen that the amount of water is more significant at 40 °C compared to 60 °C, as discussed earlier in the Raman results. By the same token, the intensity of the CO_2 peaks put in evidence the lower density of CO_2 at 60 °C ($\rho(CO_2, 60\,°C) = 290\ kg/m^3$) compared to 40 °C ($\rho(CO_2, 40\,°C) = 630\ kg/m^3$) at the same pressure. The 10-minute measurements were chosen as references for the rest of the in-situ spectra since no other species were detected at this point in the treatment. It was also a sufficient time to ensure homogeneous mixing of the water into the $scCO_2$. The final processed spectra for the in-situ measurements at 40 °C and treatment times of 30, 60, 90 and 120 min are shown in Fig. 8.

The 40 °C sample shows the emergence of a peak at 1390 cm^{-1} that is typical for ν_3 antisymmetric stretching of CO_3^{2-} for $ZnCO_3$ [26]. The measurements show that the carbonate formation started between 60- and 90-minutes holding times. Although FTIR or Raman signal of the corrosion products was not detected in the early stages of the treatment, the formation likely started earlier as visually observed from the in-situ images (Fig. 3). Liquid water was not detected on the surface during the treatment period. However, it is likely that a small water layer is present on the zinc surface to enable carbonate growth. Due to prior observation about the insensitivity of Raman and FTIR to small amounts of carbonates, the signal from a minute liquid water film on the zinc surface could also be challenging to detect. The 60 °C sample did not show any significant formation of carbonates in the FTIR spectra similarly as in Raman tests (Fig. S1, supporting information). The FTIR results are in good agreement with the earlier Raman measurements and confirm that the carbonate forms similarly even on a larger scale on the zinc surface.

In-situ FTIR spectra were also recorded during the depressurization after the 120-minute treatment (Fig. 9). The influence of CO_2 or dissolved water was not eliminated in these spectra so that the total behaviour of depressurization could be observed. Along with the wavenumber range 1150 – 2150 cm^{-1} also the OH-region between 3000 – 3500 cm^{-1} is presented.

The 40 °C spectrum shows a decrease in CO_2 pressure as the peaks 2070 cm^{-1} and 1300 cm^{-1} reduce in intensity. The overlapping peak of CO_2 and $ZnCO_3$ at 1390 cm^{-1} decreases in intensity when CO_2 pressure decreases. However, the peak remains after CO_2 removal showing $ZnCO_3$ presence. The intensity of the dissolved water peak at 1607 cm^{-1} is decreasing accordingly, and a slight peak at 1650 cm^{-1} can be seen during 5 – 15 min of depressurization. This peak corresponds to the presence of liquid water which is further confirmed by the emergence of a broad peak at 3200 cm^{-1} which is the vibration of OH-groups in water [23]. Liquid water appears when the dissolved water in the $scCO_2$ phase starts to precipitate as water [33]. The precipitation of water is a result of the decreasing solubility of water in $scCO_2$ as the pressure and temperature drop, especially below the supercritical point (74 bar, 31 °C). As the saturation level of the dissolved water drops, it starts to precipitate inside the pressure cell. Towards the end of depressurization, the liquid water peak and OH-vibration have

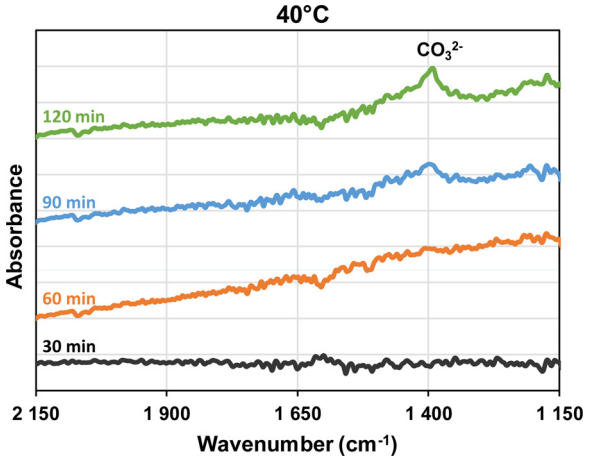

Fig. 8. In-situ FTIR spectra at 30, 60, 90 and 120 min holding times of Zn samples in wet $scCO_2$ at 100 bar pressure and treatment temperature of 40 °C. The spectra have been processed by subtracting the 10-minute spectrum.

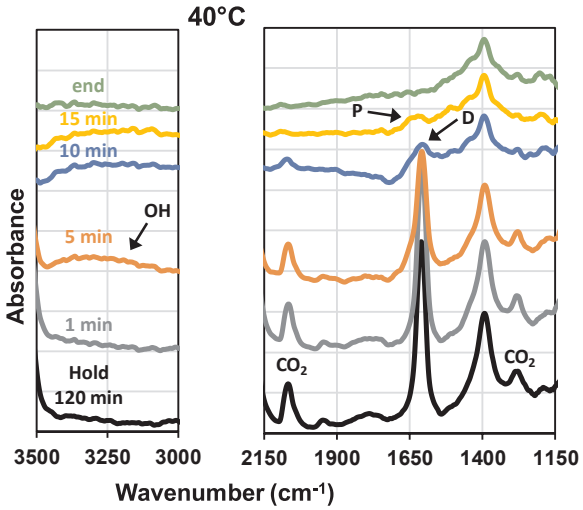

Fig. 9. In-situ spectra of FTIR 40 °C sample during depressurization. Letter "D" denotes dissolved water, and "P" precipitated water.

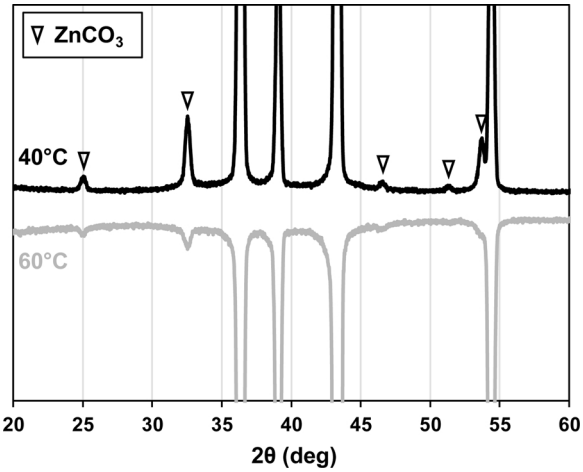

Fig. 10. XRD spectra of in-situ Raman samples. The unmarked peaks are characteristic of metallic zinc.

disappeared. Water could not be detected after all CO_2 had been removed, and therefore no significant amount of the precipitated water came in contact with the zinc surface. Consequently, the majority of the precipitated water likely stayed in between the window and the sample and had a negligible effect on the zinc surface. However, a thicker water layer that forms with higher amounts of precipitation might affect the zinc surface more significantly, which is studied in the following chapter.

The XRD results of the Raman samples are shown in Fig. 10. The XRD peaks indicate the presence of $ZnCO_3$ and metallic zinc from the substrate in all samples, which confirms the earlier Raman and FTIR results. XRD measurements of the FTIR samples showed identical results. Since no other carbonate species was observed, the formation of anhydrous $ZnCO_3$ on zinc is the prevalent reaction in wet $scCO_2$ phase.

3.2. In-situ sessile droplet tests (Raman)

We previously observed a needle-like zinc hydroxy carbonate species in similar treatment conditions which did not form in the $scCO_2$ tests performed here [10,11,34–36]. Higher amounts of water precipitation compared to this study have shown to impact the corrosion of the sample surface in other studies during depressurization of $scCO_2$ [29,37,38]. Therefore, the effect of a water layer on zinc in pressurized CO_2 was investigated further with sessile droplet tests. As dissolved oxygen in water has been shown to affect the corrosion of zinc considerably due to its significant role in cathodic action [7,39], the effect of O_2 gas addition was investigated as well.

The SEM images of the in-situ tests performed at 5 bar of CO_2 and 22 °C (room temperature) are shown in Fig. 11. Sample A is without extra oxygen and sample B with the addition of 2 bar of O_2. Additionally, the same tests were performed at 40 °C temperature. The reaction conditions simulated the end of the depressurization phase of the $scCO_2$ treatments. A needle-like structure arranged in flower shapes is observed in both samples. The needle-structure covers the entire droplet area in sample B with oxygen, whereas some areas of the surface of sample A remain exposed. The partial pressure of oxygen in the reaction for sample B is ten times higher than for sample A that is only exposed to one atmospheric pressure of air that remained in the cell after CO_2 addition. Consequently, the availability of the dissolving oxygen in sample A diminishes, resulting in decreased reactivity due to insufficient cathodic action. Sample A also shows the presence of spherical structures on the zinc surface which might be hidden under the needle structure in sample B. The needle structure was much more prevalent compared to the spherical structure. The main difference in the 40 °C samples (Fig. S3, supporting information) compared to the 22 °C samples was more presence of the spherical structure instead of the needle structure. The morphology of the structures observed here in this study is identical to species shown in our previous studies, where the structures formed under $scCO_2$ conditions [10,11,34–36]. Corrosion products are not observed outside the droplet area without the presence of water in the CO_2 phase. As discussed earlier, the water dissolved in $scCO_2$ induced growth of $ZnCO_3$ in the immediate proximity of the zinc surface. Conversely, CO_2 dissolved in a thick water layer resulted in the growth of the needle-like structure. The needle-like structure protrudes significantly from the surface [11] but not outside the droplet. Therefore, a thick water film is required for the needle-like structure to grow, which further explains its absence in the $scCO_2$ phase.

Fig. 12 shows the in-situ optical images for samples A and B taken from the middle of the droplet. Dark deposits appear rapidly on sample B during the first 10 min. In contrast, only small changes occurred in sample A at the same time. Raman spectrum taken at 5 min from the middle of the image of sample B corresponds to ZnO (Fig. 13). Consequently, the oxygen addition accelerated the corrosion process considerably in the early stages of the test. However, both samples showed considerable reactivity at 60 min based on visual appearance.

The in-situ spectra of sample B are presented in Fig. 13. ZnO has not formed without the presence of CO_2 or O_2 as seen from the first spectrum (No CO_2) which is taken just before the introduction of the gases. However, ZnO forms rapidly within the first 5 min of the experiment. The presence of ZnO continues until 45 min into the treatment without the presence of other species. Subsequently, a peak at 1099 cm^{-1} emerges that was identified as the needle structure. The in-situ tests confirmed that the formation of $ZnCO_3$ also occurred in the later stages of the experiment (Fig. S4, supporting information). The delayed formation of the carbonates is consistent in all samples, which is likely due to insufficient CO_2 concentration early in the experiment. The diffusion of CO_2 is relatively slow in water [40] and limits the reaction for the carbonate formation. The ZnO peak diminishes as the reaction progresses and disappears when the needle structure starts to grow. The conversion of ZnO to carbonate indicates that ZnO acts as an intermediate corrosion product, as was discussed earlier in the $scCO_2$ section.

The ex-situ Raman spectra of the structures in sample A are presented in Fig. 14. The results show the presence of peaks 300 cm^{-1}, 730 cm^{-1} and 1093 cm^{-1} which correspond to $ZnCO_3$ and a peak at 570 cm^{-1} previously identified as nanosized ZnO. The needle structure had a different spectrum as the spherical structure with only a single distinct peak at 1099 cm^{-1} that had a shoulder peak at 1049 cm^{-1} as well as lower intensity peaks at 235 cm^{-1} and 390 cm^{-1}. The spectra of both structures were well in accordance with our earlier study on the same structures [11].

The XRD of the needle structure and hydrozincite reference are shown in Fig. 15. The spectrum does not match to any common zinc hydroxy carbonates, i.e. hydrozincite. However, the spectrum closely resembles structures zinc hydroxy carbonates synthesized by various techniques in other studies [41–44]. These studies, as well as our earlier characterizations, expect the chemical structure of the needles to be hydrated zinc hydroxy carbonate of form $Zn_a(CO_3)_b(OH)_c{\cdot}dH_2O$. However, the exact stoichiometric composition remains unknown.

Illustration of the reactions occurring inside the droplet is presented in Fig. 16. Three main reactions take place in the formation of the reaction products.

1 Zn^{2+} dissolution (Anodic reaction)
2 O_2 dissolution (Cathodic reaction)
3 CO_2 dissolution resulting in the formation of carbonic acid

Zinc dissolution is required for any zinc corrosion product formation. This anodic activity must be balanced by a cathodic reaction that could be either hydrogen gas evolution or dissolution of oxygen from the surroundings. The common cathodic reaction for corrosion of zinc is

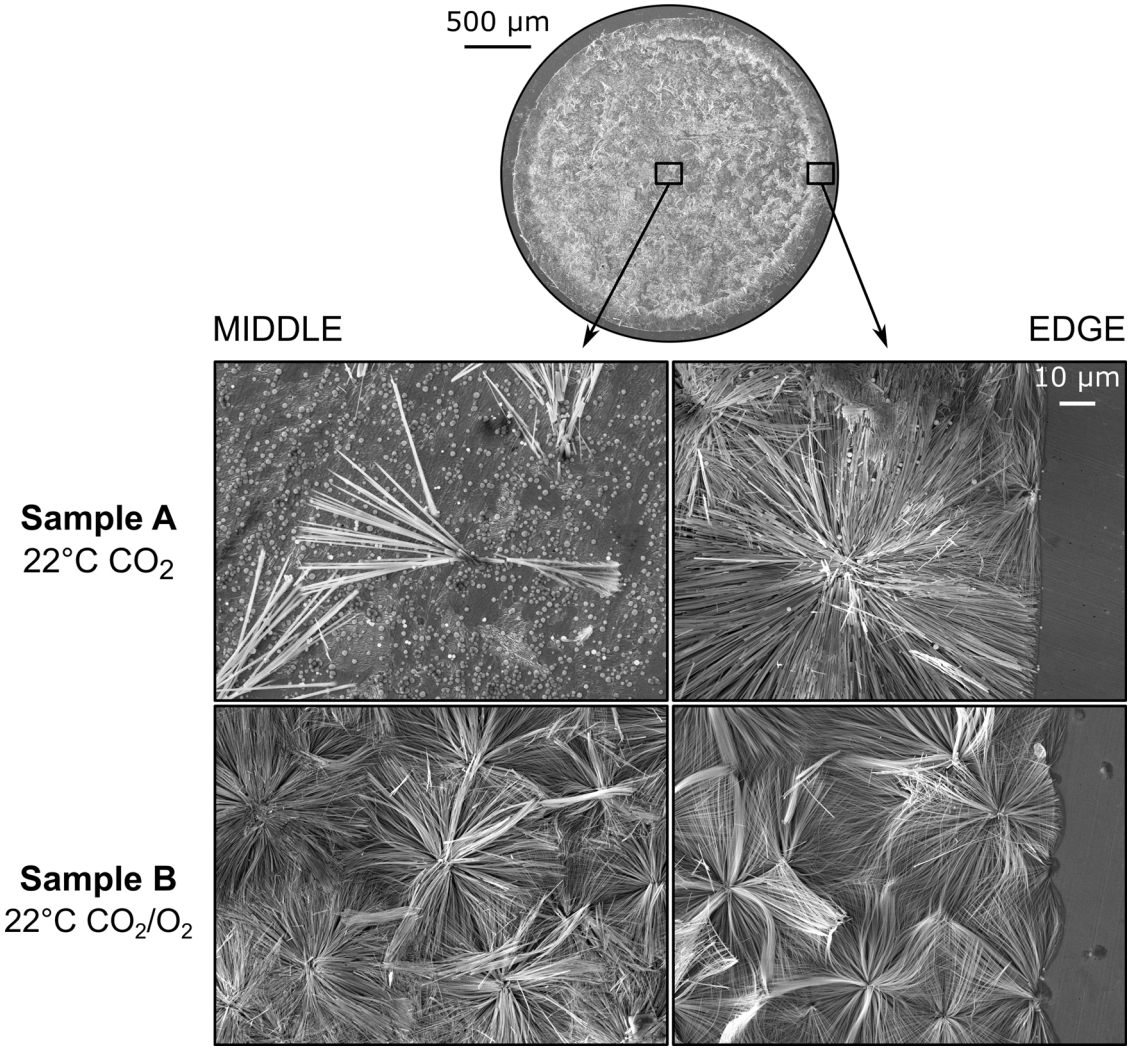

Fig. 11. SEM images of the droplet experiment of sample A and sample B. The upper droplet image (Sample A) shows where the middle and edge droplet images were taken. The left and right images show the higher magnification images of the middle and edge of the droplet, respectively.

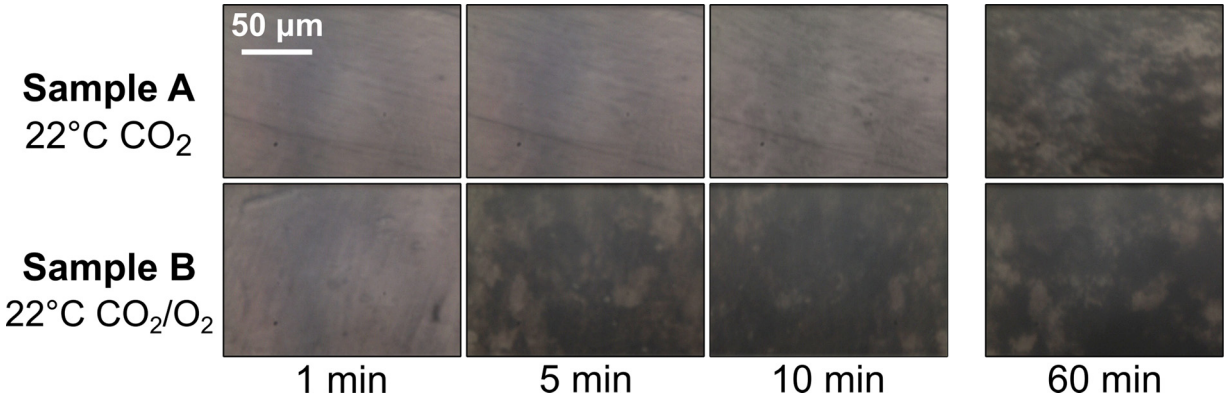

Fig. 12. In-situ optical images of sample A and sample B from the middle of the water droplet.

typically oxygen dissolution according to earlier studies [7,8,45,46]. As the oxygen dissolves, it reacts with water and produces hydroxyl-ions (OH^-). The drastic effect of oxygen seen in sample B supports the accelerative effect on the reactions as a result of increased cathodic action that leads to Zn^{2+} ion dissolution. Some hydrogen evolution could also be possible due to acidic conditions and much lower availability of oxygen in sample A. The oxygen dissolution in the droplets occurs at the outer edge which usually results in higher cathodic activity and alkalinity at the edge of the droplet. Conversely, oxygen depletion and its insufficient diffusion rate to replace the oxygen causes higher anodic activity in the middle region of the droplet [45–47]. As was seen from the SEM images (Fig. 11), more needle structure concentrated at the edge areas rather than the middle of the droplet. As the oxygen content in sample A is limited, the reaction is likely to occur at the edges where is better availability of all reaction constituents, CO_2 and O_2.

As the Zn^{2+} ion concentration increases inside the droplet, they

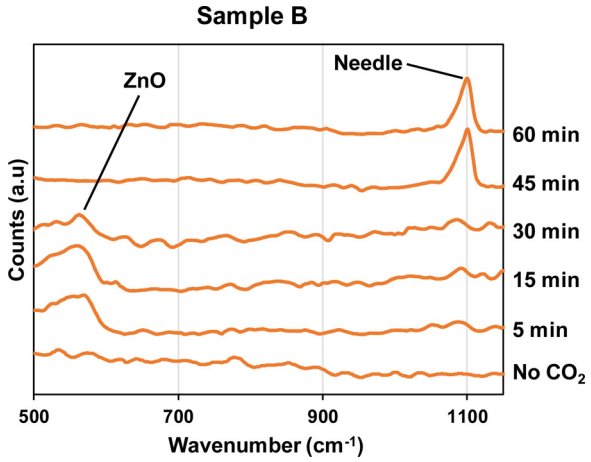

Fig. 13. In-situ Raman measurements of sample B from the middle of the water droplet (centre of Fig. 12).

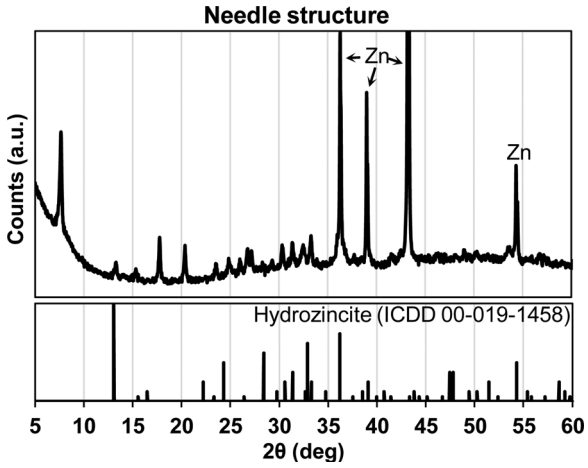

Fig. 15. XRD spectrum of the needle structure (with residual metallic zinc) separated from the surface. The spectrum of hydrozincite is presented as a reference.

start to react together to form ZnO. It is commonly known that also zinc hydroxide ($Zn(OH)_2$) is one of the main corrosion products of zinc that could form either before, after or simultaneously with ZnO [7,48,49]. In a study by Ohtsuka et al., they detected the formation of both ZnO and $Zn(OH)_2$ by in-situ Raman investigations in atmospheric conditions [14]. However, the measurements in our study did not detect $Zn(OH)_2$. Since high CO_2 concentration leads to acidic conditions with approximate water pH of 3–4 [50], the absence of $Zn(OH)_2$ precipitates could be due to high CO_2 concentration as it is more stable at alkaline conditions [51,52]. After the formation of ZnO, it likely reacts with the dissociated carbonic acid to form $ZnCO_3$ and $Zn_a(CO_3)_b(OH)_c{\cdot}dH_2O$. The conversion of ZnO to carbonates is further supported by a study where ZnO powder was converted into zinc hydroxy carbonate under humid CO_2 atmosphere [53]. The reaction could proceed by either redissolution and precipitation, or directly with the HCO_3^- and CO_3^{2-} ions [54].

The needle structure was the prevalent reaction product compared to $ZnCO_3$ in room temperature. Similar zinc hydroxy carbonate structures have been shown to be more stable compounds in lower temperatures [42]. Furthermore, Hu et al. showed the formation of similar needle structures in lower temperatures but resulted in spherical structures, similar to $ZnCO_3$, in higher temperatures when anodizing zinc foils [55].

Diffusion of the gaseous species, CO_2 and O_2, crucially affects the supply of the ionic species required for the formation of the corrosion products in the droplet experiments. The initial reactivity of the surface was significantly accelerated when O_2 was added due to increased cathodic activity that facilitated Zn^{2+} dissolution. Nevertheless, mainly ZnO was present in the early stages of the experiments with only little carbonates formed. The diffusion of CO_2 limits the carbonate formation and only in the latter part of the experiment, the carbonates started to fully develop. Although diffusion is an essential factor in the droplet experiments, it has less effect in the depressurization phase of the $scCO_2$ treatments where the precipitation of water could result in carbonate formation as well. During depressurization, the droplets forming from the precipitated water are immediately saturated by the surrounding gases because of their small size [56]. Consequently, more rapid formation of the carbonates as seen in our previous studies is possible during the depressurization phase of the $scCO_2$ treatment compared to the droplet experiments shown in this study [11,34–36].

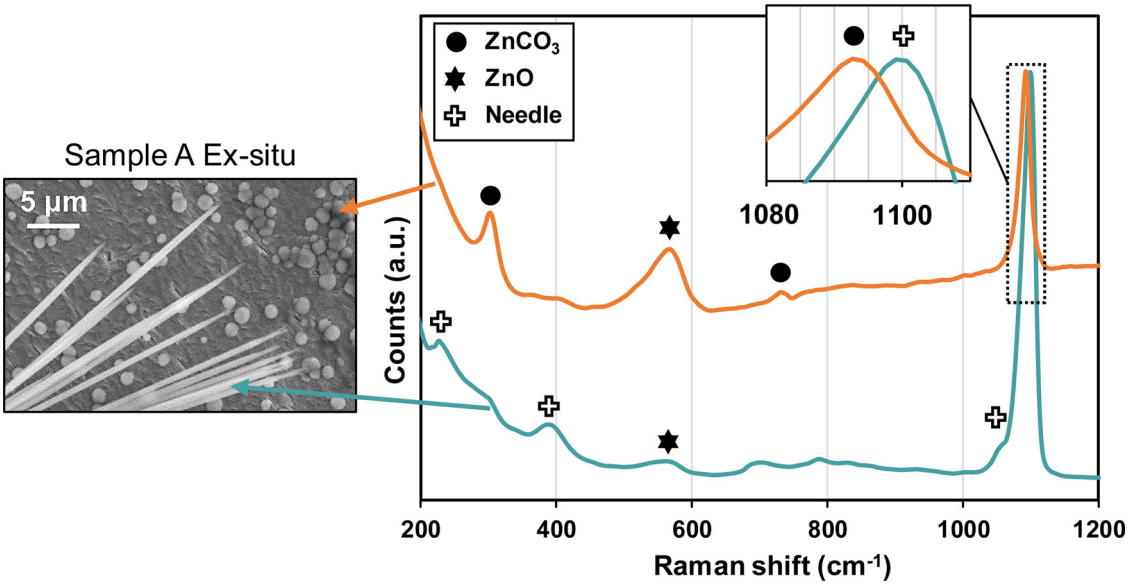

Fig. 14. Ex-situ Raman spectra of sample A (22 °C with CO_2).

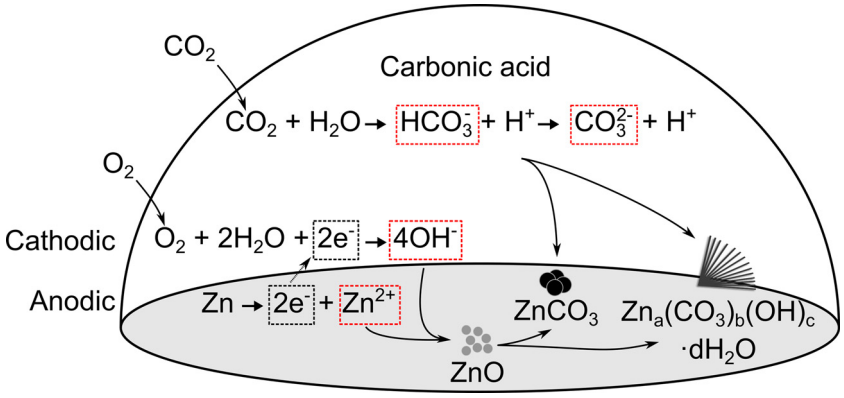

Fig. 16. Reactions involved in the droplet for carbonate formation.

4. Conclusions

The effect of wet $scCO_2$ treatments on zinc surfaces was investigated with in-situ optical imaging, Raman and FTIR. The study aimed to obtain an overview of the reactions involved in the formation of corrosion products in $scCO_2$ phase and the following depressurization in the pretreatment. It was also shown that Raman and FTIR suited well for the in-situ characterization of the corrosion products and reaction kinetics.

The tests in wet $scCO_2$ showed the growth of $ZnCO_3$ and a presence of ZnO on the zinc surface during the treatments. According to the optical images, distinct dark spatters appeared on the zinc surface as initiation points for the corrosion products and gradually increased in quantity as the treatment progressed. $ZnCO_3$ eventually formed on these areas. This behaviour was homogeneous throughout the surface, which was confirmed by the FTIR results and SEM observations. The $ZnCO_3$ formation was more prevalent in 40 °C compared to 60 °C due to the higher amount of dissolved water in the $scCO_2$.

The dissolved water in the $scCO_2$ phase precipitated as a liquid water layer during the depressurization of the cell. Thus, in order to simulate the depressurization phase in the $scCO_2$ treatment, the effect of liquid water on the zinc surface was investigated further by sessile droplet tests at lower temperatures and pressures. ZnO formed in the initial stages of the experiments. As the experiment progressed, the droplet tests showed the growth of $ZnCO_3$ and a needle-like structure that was not observed in $scCO_2$. Initial ZnO formation followed by carbonate formation could indicate the conversion of the ZnO to the carbonate structures. The role of oxygen was important for the reaction as it significantly increased the rate of zinc ion dissolution by enhancing cathodic action. The carbonate species formed only in the later stages of the experiments, which was likely due to a limited rate of CO_2 diffusion. However, the diffusion rate is not expected to be a limiting factor in the depressurization phase of $scCO_2$ treatment due to much shorter diffusion lengths and continuously increasing droplet size.

The presence of a water layer is paramount for the formation of both carbonate structures. Although the role of $scCO_2$ phase is less pronounced for the actual carbonate formation, it enables the growth of the carbonates as well as the contact of the precipitated water to reach all surfaces throughout the cell volume during the depressurization.

Data availability

The raw/processed data required to reproduce these findings cannot be shared at this time due to technical or time limitations.

CRediT authorship contribution statement

A. Kaleva: Conceptualization, Methodology, Investigation, Writing - original draft. **T. Tassaing:** Resources, Validation. **V. Saarimaa:** Resources, Writing - review & editing. **G. Le Bourdon:** Resources, Data curation. **P. Väisänen:** Funding acquisition, Writing - review & editing. **A. Markkula:** Funding acquisition, Writing - review & editing. **E. Levänen:** Supervision.

Declaration of Competing Interest

The authors declare that they have no known competing financial interests or personal relationships that could have appeared to influence the work reported in this paper.

Acknowledgements

This work was carried out through the doctoral school of industrial innovations (DSII) program as part of the research activities of Tampere University with financial support from SSAB Europe which is gratefully acknowledged.

Appendix A. Supplementary data

Supplementary material related to this article can be found, in the online version, at doi:https://doi.org/10.1016/j.corsci.2020.108850.

References

[1] X. Zhang, Cr(VI) And Cr(III)-Based Conversion Coatings on Zinc, Hunan University, 2005.
[2] P. Puomi, H.M. Fagerholm, J.B. Rosenholm, K. Jyrkäs, Comparison of different commercial pretreatment methods for hot-dip galvanized and Galfan coated steel, Surf. Coatings Technol. 115 (1999) 70–78, https://doi.org/10.1016/S0257-8972(99)00170-X.
[3] O. Gharbi, S. Thomas, C. Smith, N. Birbilis, Chromate replacement: what does the future hold? Npj Mater. Degrad. 2 (2018) 12, https://doi.org/10.1038/s41529-018-0034-5.
[4] T.S.N.S. Narayanan, Surface pretreatment by phosphate conversion coatings - a review, Rev. Adv. Mater. Sci. 9 (2005) 130–177.
[5] J.F. Malone, Painting hot-dip galvanized sheet, Mater. Perform. 31 (1992) 39–42.
[6] I. Cabanelas, A. Collazo, M. Izquierdo, X.R. Nóvoa, C. Pérez, Influence of galvanised surface state on the duplex systems behaviour, Corros. Sci. 49 (2007) 1816–1832, https://doi.org/10.1016/j.corsci.2006.10.018.
[7] X.G. Zhang, Corrosion and Electrochemistry of Zinc, Springer US, Boston, MA, 1996, https://doi.org/10.1007/978-1-4757-9877-7.
[8] J.D. Yoo, K. Ogle, P. Volovitch, The effect of synthetic zinc corrosion products on corrosion of electrogalvanized steel: I. Cathodic reactivity under zinc corrosion products, Corros. Sci. 81 (2014) 11–20, https://doi.org/10.1016/j.corsci.2013.11.045.
[9] W. He, I. Odnevall Wallinder, C. Leygraf, A laboratory study of copper and zinc runoff during first flush and steady-state conditions, Corros. Sci. 43 (2001) 127–146, https://doi.org/10.1016/S0010-938X(00)00066-4.
[10] V. Saarimaa, A. Kaleva, J.-P. Nikkanen, S. Heinonen, E. Levänen, P. Väisänen, A. Markkula, J. Juhanoja, Supercritical carbon dioxide treatment of hot dip galvanized steel as a surface treatment before coating, Surf. Coatings Technol. 331 (2017) 137–142, https://doi.org/10.1016/j.surfcoat.2017.10.047.
[11] V. Saarimaa, A. Kaleva, J.P. Nikkanen, J. Manni, C. Lange, T. Paunikallio, T. Laihinen, S. Heinonen, E. Levänen, P. Väisänen, A. Markkula, Tailoring of versatile surface morphologies on hot dip galvanized steel in wet CO2: aspects on

formation, barrier properties, and utilization as a substrate for coatings, ACS Appl. Mater. Interfaces 10 (2018) 21730–21739, https://doi.org/10.1021/acsami.8b05034.
[12] D. Lindström, I. Odnevall Wallinder, Long-term use of galvanized steel in external applications. Aspects of patina formation, zinc runoff, barrier properties of surface treatments, and coatings and environmental fate, Environ. Monit. Assess. 173 (2011) 139–153, https://doi.org/10.1007/s10661-010-1377-8.
[13] A.M. Beccaria, Zinc layer characterization on galvanized steel by chemical methods, Corrosion 46 (1990) 906–912, https://doi.org/10.5006/1.3580857.
[14] T. Ohtsuka, M. Matsuda, In situ Raman spectroscopy for corrosion products of zinc in humidified atmosphere in the presence of sodium chloride precipitate, Corrosion 59 (2003) 407–413, https://doi.org/10.5006/1.3277572.
[15] F. Zhu, D. Persson, D. Thierry, Formation of corrosion products an open and confined metal surfaces exposed to periodic wet/dry conditions - a comparison between zinc and electrogalvanized steel, Corrosion 57 (2001) 582–590, https://doi.org/10.5006/1.3280514.
[16] T. Falk, J.-E. Svensson, L.-G. Johansson, The role of carbon dioxide in the atmospheric corrosion of zinc, J. Electrochem. Soc. 145 (1998) 39–44, https://doi.org/10.1149/1.1838207.
[17] R. Lindström, J.-E. Svensson, L.-G. Johansson, The atmospheric corrosion of zinc in the presence of NaCl - the influence of carbon dioxide and temperature, J. Electrochem. Soc. 147 (2000) 1751–1757, https://doi.org/10.1149/1.1393429.
[18] R.M. Cuéllar-Franca, A. Azapagic, Carbon capture, storage and utilisation technologies: a critical analysis and comparison of their life cycle environmental impacts, J. CO2 Util. 9 (2015) 82–102, https://doi.org/10.1016/j.jcou.2014.12.001.
[19] T. Bruhn, H. Naims, B. Olfe-Kräutlein, Separating the debate on CO2 utilisation from carbon capture and storage, Environ. Sci. Policy 60 (2016) 38–43, https://doi.org/10.1016/j.envsci.2016.03.001.
[20] Y.S. Choi, S. Nešić, Determining the corrosive potential of CO2 transport pipeline in high pCO2-water environments, Int. J. Greenh. Gas Control. 5 (2011) 788–797, https://doi.org/10.1016/j.ijggc.2010.11.008.
[21] C. Quilfen, T. Tassaing, D. Uzio, C. Aymonier, In situ Raman investigation of the preparation of HDS catalyst precursors using scCO2, J. Supercrit. Fluids 141 (2018) 104–112, https://doi.org/10.1016/j.supflu.2017.12.018.
[22] V. Prigiobbe, M. Hänchen, M. Werner, R. Baciocchi, M. Mazzotti, Mineral carbonation process for CO2 sequestration, Energy Procedia 1 (2009) 4885–4890, https://doi.org/10.1016/j.egypro.2009.02.318.
[23] J.S. Loring, C.J. Thompson, Z. Wang, A.G. Joly, D.S. Sklarew, H.T. Schaef, E.S. Ilton, K.M. Rosso, A.R. Felmy, In situ infrared spectroscopic study of forsterite carbonation in wet supercritical CO 2, Environ. Sci. Technol. 45 (2011) 6204–6210, https://doi.org/10.1021/es201284e.
[24] N. Spycher, K. Pruess, J. Ennis-King, CO2-H2O mixtures in the geological sequestration of CO2. I. Assessment and calculation of mutual solubilities from 12 to 100°C and up to 600 bar, Geochim. Cosmochim. Acta 67 (2003) 3015–3031, https://doi.org/10.1016/S0016-7037(03)00273-4.
[25] M. Champeau, J.-M. Thomassin, C. Jérôme, T. Tassaing, In situ FTIR micro-spectroscopy to investigate polymeric fibers under supercritical carbon dioxide: CO2 sorption and swelling measurements, J. Supercrit. Fluids 90 (2014) 44–52, https://doi.org/10.1016/j.supflu.2014.03.006.
[26] M.C. Hales, R.L. Frost, Synthesis and vibrational spectroscopic characterisation of synthetic hydrozincite and smithsonite, Polyhedron 26 (2007) 4955–4962, https://doi.org/10.1016/j.poly.2007.07.002.
[27] W. Bin Cai, D.A. Scherson, In situ Raman spectroscopy of zinc electrodes in alkaline solutions, J. Electrochem. Soc. 150 (2003) 217–223, https://doi.org/10.1149/1.1563651.
[28] A. Rumyantseva, S. Kostcheev, P.-M. Adam, S.V. Gaponenko, S.V. Vaschenko, O.S. Kulakovich, A.A. Ramanenka, D.V. Guzatov, D. Korbutyak, V. Dzhagan, A. Stroyuk, V. Shvalagin, Nonresonant surface-enhanced Raman scattering of ZnO quantum dots with Au and Ag nanoparticles, ACS Nano 7 (2013) 3420–3426, https://doi.org/10.1021/nn400307a.
[29] M. Xu, W. Li, Y. Zhou, X.X. Yang, Z. Wang, Z. Li, Effect of pressure on corrosion behavior of X60, X65, X70, and X80 carbon steels in water-unsaturated supercritical CO2 environments, Int. J. Greenh. Gas Control 51 (2016) 357–368, https://doi.org/10.1016/j.ijggc.2016.06.002.
[30] A.Q. Liu, C. Bian, Z.M. Wang, X. Han, J. Zhang, Flow dependence of steel corrosion in supercritical CO2 environments with different water concentrations, Corros. Sci. 134 (2018) 149–161, https://doi.org/10.1016/j.corsci.2018.02.027.
[31] G.L. Cox, Effect of temperature on the corrosion of zinc, Ind. Eng. Chem. 23 (1931) 902–904, https://doi.org/10.1021/ie50260a011.
[32] J.S. Loring, C.J. Thompson, Z. Wang, A.G. Joly, D.S. Sklarew, H.T. Schaef, E.S. Ilton, K.M. Rosso, A.R. Felmy, In situ infrared spectroscopic study of forsterite carbonation in wet supercritical CO2, Environ. Sci. Technol. 45 (2011) 6204–6210, https://doi.org/10.1021/es201284e.
[33] Y. Hua, R. Barker, T. Charpentier, M. Ward, A. Neville, Relating iron carbonate morphology to corrosion characteristics for water-saturated supercritical CO2 systems, J. Supercrit. Fluids 98 (2015) 183–193, https://doi.org/10.1016/j.supflu.2014.12.009.
[34] A. Kaleva, V. Saarimaa, S. Heinonen, J.-P. Nikkanen, A. Markkula, P. Väisänen, E. Levänen, Dissolution-induced nanowire synthesis on hot-dip galvanized surface in supercritical carbon dioxide, Nanomaterials. 7 (2017) 181, https://doi.org/10.3390/nano7070181.
[35] A. Kaleva, J.-P. Nikkanen, S. Heinonen, V. Saarimaa, T. Vuorinen, M. Honkanen, L. Hyvärinen, E. Levänen, Synthesis of ZnO nanowires with supercritical carbon dioxide and post heat treatment, Nanotechnology 29 (2018), https://doi.org/10.1088/1361-6528/aada69 445601.
[36] J.-P. Nikkanen, S. Heinonen, P. Väisänen, V. Saarimaa, A. Markkula, T. Paunikallio, A. Kaleva, E. Levänen, Convenient extraction method for quantification of thin zinc patina layers, Surf. Interface Anal. 50 (2018) 564–570, https://doi.org/10.1002/sia.6429.
[37] Y. Hua, S. Mohammed, R. Barker, A. Neville, Comparisons of corrosion behaviour for X65 and low Cr steels in high pressure CO2-saturated brine, J. Mater. Sci. Technol. 41 (2020) 21–32, https://doi.org/10.1016/j.jmst.2019.08.050.
[38] A. Dugstad, M. Halseid, B. Morland, A.O. Sivertsen, Corrosion in dense phase CO2 - the impact of depressurisation and accumulation of impurities, Energy Procedia 37 (2013) 3057–3067, https://doi.org/10.1016/j.egypro.2013.06.192.
[39] S. Sarrade, D. Féron, F. Rouillard, S. Perrin, R. Robin, J.C. Ruiz, H.A. Turc, Overview on corrosion in supercritical fluids, J. Supercrit. Fluids 120 (2017) 335–344, https://doi.org/10.1016/j.supflu.2016.07.022.
[40] C. Belgodere, J. Dubessy, D. Vautrin, M.C. Caumon, J. Sterpenich, J. Pironon, P. Robert, A. Randi, J.P. Birat, Experimental determination of CO2 diffusion coefficient in aqueous solutions under pressure at room temperature via Raman spectroscopy: impact of salinity (NaCl), J. Raman Spectrosc. 46 (2015) 1025–1032, https://doi.org/10.1002/jrs.4742.
[41] D.O. Miles, P.J. Cameron, D. Mattia, Hierarchical 3D ZnO nanowire structures via fast anodization of zinc, J. Mater. Chem. A 3 (2015) 17569–17577, https://doi.org/10.1039/C5TA03578C.
[42] Y. Sawada, M. Murakami, T. Nishide, Thermal analysis of basic zinc carbonate. Part 1. Carbonation process of zinc oxide powders at 8 and 13°C, Thermochim. Acta 273 (1996) 95–102, https://doi.org/10.1016/0040-6031(95)02631-2.
[43] S. Zhang, H. Fortier, J.R. Dahn, Characterization of zinc carbonate hydroxides synthesized by precipitation from zinc acetate and potassium carbonate solutions, Mater. Res. Bull. 39 (2004) 1939–1948, https://doi.org/10.1016/j.materresbull.2004.05.023.
[44] N. Ohkuma, Y. Funayama, H. Ito, N. Mizutani, M. Kato, Reaction of carbon dioxide containing water vapor with ZnO fine particles, Nippon. Kagaku Kaishi 53 (1987) 802–806, https://doi.org/10.1246/nikkashi.1987.802.
[45] R.J. Jiang, Y.F. Cheng, Mechanism of electrochemical corrosion of steel under water drop, Electrochem. Commun. 35 (2013) 8–11, https://doi.org/10.1016/j.elecom.2013.07.019.
[46] T.H. Muster, A. Bradbury, A. Trinchi, I.S. Cole, T. Markley, D. Lau, S. Dligatch, A. Bendavid, P. Martin, The atmospheric corrosion of zinc: the effects of salt concentration, droplet size and droplet shape, Electrochim. Acta 56 (2011) 1866–1873, https://doi.org/10.1016/j.electacta.2010.09.099.
[47] N.S. Azmat, K.D. Ralston, B.C. Muddle, I.S. Cole, Corrosion of Zn under acidified marine droplets, Corros. Sci. 53 (2011) 1604–1615, https://doi.org/10.1016/j.corsci.2011.01.044.
[48] E. Diler, B. Lescop, S. Rioual, G. Nguyen Vien, D. Thierry, B. Rouvellou, Initial formation of corrosion products on pure zinc and MgZn2 examinated by XPS, Corros. Sci. 79 (2014) 83–88, https://doi.org/10.1016/j.corsci.2013.10.029.
[49] I. Odnevall Wallinder, C. Leygraf, A critical review on corrosion and runoff from zinc and zinc-based alloys in atmospheric environments, Corrosion 73 (2017) 1016–1077, https://doi.org/10.5006/2458.
[50] B. Meyssami, M.O. Balaban, A.A. Teixeira, Prediction of pH in model systems pressurized with carbon dioxide, Biotechnol. Prog. 8 (1992) 149–154, https://doi.org/10.1021/bp00014a009.
[51] R.A. Reichle, K.G. McCurdy, L.G. Hepler, Zinc Hydroxide, Solubility product and hydroxy-complex stability constants from 12.5–75 °C, Can. J. Chem. 53 (1975) 3841–3845, https://doi.org/10.1139/v75-556.
[52] A. Krężel, W. Maret, The biological inorganic chemistry of zinc ions, Arch. Biochem. Biophys. 611 (2016) 3–19, https://doi.org/10.1016/j.abb.2016.04.010.
[53] E. Turianicová, M. Káňuchová, A. Zorkovská, M. Holub, Z. Bujnáková, E. Dutková, M. Baláz, L. Findoráková, M. Balintová, A. Obut, CO2 utilization for fast preparation of nanocrystalline hydrozincite, J. CO2 Util. 16 (2016) 328–335, https://doi.org/10.1016/j.jcou.2016.08.007.
[54] I. Odnevall, Atmospheric Corrosion of Field Exposed Zinc, Royal Institute of Technology, 1994.
[55] Z. Hu, Q. Chen, Z. Li, Y. Yu, L.M. Peng, Large-scale and rapid synthesis of ultralong ZnO nanowire films via anodization, J. Phys. Chem. C 114 (2010) 881–889, https://doi.org/10.1021/jp9094744.
[56] N.S. Azmat, K.D. Ralston, B.C. Muddle, I.S. Cole, Corrosion of Zn under fine size aerosols and droplets using inkjet printer deposition and optical profilometry quantification, Corros. Sci. 53 (2011) 3534–3541, https://doi.org/10.1016/j.corsci.2011.06.028.